Ultrathin Magnetite in Fe_3O_4/MgO super-lattices – investigating the enhanced, thin film magnetic moment

Ozhet Mauit,[1, 2, *] Karsten Fleischer,[1, †] Cormac Ó Coileáin,[1, 3] Brendan Bulfin,[4] Daniel S. Fox,[1] Christopher M. Smith,[1] Daragh Mullarkey,[1] Gulnar Sugurbekova,[2] Hongzhou Zhang,[1] and Igor V. Shvets[1]

[1] School of Physics and CRANN, Trinity College Dublin, The University of Dublin, Ireland
[2] National Laboratory Astana, Nazarbayev University, Astana, Kazakhstan
[3] KSU-Aramco Center, King Saud University, Riyadh 11451, Saudi Arabia
[4] Institute of Solar Research, German Aerospace Center (DLR), 51147 Köln, Germany
(Dated: March 27, 2017)

The electrical, crystallographic and magnetic properties of ultra-thin magnetite (Fe_3O_4) have been studied in detail, by employing superlattice structures of Fe_3O_4/$MgFe_2O_4$ and Fe_3O_4/MgO on a variety of substrates. By careful analysis of their properties, the influence of substrate stoichiometry, Fe_3O_4 thin film thickness, antiphase boundaries on the magnetic properties can be separated. In particular, the controversial enhanced magnetic moment in ultra-thin films (<5 nm) was confirmed to be related to the substrate stoichiometry, specifically the migration of oxygen vacancies into the Fe_3O_4 thin films. The multilayer concept can be employed with many other such systems and offers new methods of tuning the properties of thin magnetic oxides.

INTRODUCTION

Transition metal oxides are interesting materials to study the complex interaction between electron spin, charge and orbital order. These interactions are at the heart of novel multifunctional oxides used in spin valves and other devices reliant on electron spin interaction.[1] One such oxide is magnetite (Fe_3O_4), a ferromagnet at room temperature which undergoes a metal insulator transition (Verwey transition) around 120 K.[2,3] In recent years Fe_3O_4 attracted renewed attention not just from a fundamental point of view, as the mechanism behind the Verwey transition is better understood,[3–9], but also for the observed changes in the intrinsic physical properties of ultra-thin films once the thickness is reduced to well below 10-15 nm.[10–16] For spintronic applications, particular if the oxide is used as spin filter, the oxide thickness will be only a few nm.[17] Hence any alterations of the magnetic structure in such ultrathin films is of major interest. Most noteworthy, for Fe_3O_4 an enhanced magnetic moment has been frequently observed in layers thinner than 5 nm.[11] There have been many attempts to explain the enhancement, ranging from interface magnetic moments[10,11,18] to measurement artefacts caused by a residual substrate magnetisation.[19] A combined experimental and theoretical study of oxidised thin metallic iron films grown on GaAs suggested that oxygen vacancies play a major role.[16]

We have developed an experimental approach to investigate the origin of the enhanced moment in ultra-thin Fe_3O_4 grown on oxide substrates by employing a set of stacked multilayer samples as illustrated in Fig. 1. Our primary aim was to improve the signal to noise (SNR) in magnetic measurements for ultra-thin films, by increasing the number of layers. This concept has been used previously to enhance the SNR of magnetic measurements, and to exclude the influence of interface effects on the superparamagnetic behaviour of ultra-thin Fe_3O_4 films

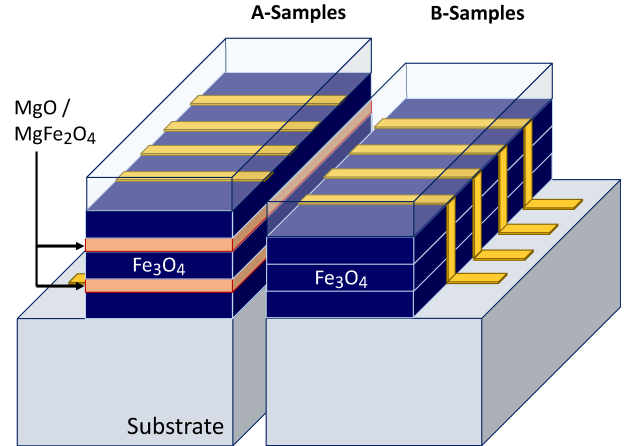FIG. 1. Schematic representation of the sample sets under investigation. Several multilayers were grown on MgO(001) and $SrTiO_3$(001) substrates. The thickness of the individual Fe_3O_4 layers was varied from 2 - 6 nm, and the spacer layers were ≈2 nm thick MgO or $MgFe_2O_4$. Half of each sample (Part B) was shadowed during the growth of the spacer layers, leading to continuous Fe_3O_4 films of 3 - 18 nm, grown simultaneously with the multilayer samples. All samples have been capped by MgO to prevent surface oxidisation and cut ex-situ to independently measure parts A and B. Gold contacts were deposited prior to capping in order to facilitate electrical characterisation.

by the use of 2 nm MgO spacers.[20] We have adapted the method to investigate the size effects by systematic variation of magnetic properties with individual Fe_3O_4 film thickness, as well as altering the material of the spacer layers. The size confinement was achieved employing not only MgO but also $MgFe_2O_4$ as spacer layers and the validity of this approach was confirmed by X-ray reflection (XRR), Raman spectroscopy, and Transmission electron micrographs (TEM) confirming the sample structure.

Using multilayers it is possible to independently alter

certain sample properties such as the density of anti-phase boundaries by replacing the MgO spacers with $MgFe_2O_4$. As growth conditions and individual substrate quality can also influence the properties of Fe_3O_4, thicker reference layers (B-Samples) were grown on the same substrate by partially shadowing the samples during the growth of the spacer layers. Our approach allowed for a direct comparison of samples having the same total Fe_3O_4 thickness (d_{Total}), with one part (A) consisting of three, separated layers with an individual Fe_3O_4 layer thickness ($d_{Fe_3O_4} = d_{Total}/3$) and uninterrupted part (B) with $d_{Fe_3O_4} = d_{Total}$ (see Fig. 1).

We will demonstrate that the substrate stoichiometry, in particular the density of oxygen vacancies, is the main cause of the frequently observed enhanced magnetic moment in ultra-thin Fe_3O_4 grown on oxides. We will also demonstrate that by employing the correct substrate treatment, with optimised growth conditions to avoid over or under oxidisation, combined with *in-situ* capping to prevent surface oxidisation during exposure[21,22], layers as thin as 5 nm still show Verwey transitions. The previously reported[23] disappearance of the transition below 20 nm is hence not an inherent property of Fe_3O_4 thin films, but rather due to changes in the sample stoichiometry induced by surface oxidisation, interface reduction or non ideal growth conditions.

I. EXPERIMENTAL DETAILS

Ultra-thin epitaxial Fe_3O_4 films with and without spacer layers of $MgFe_2O_4$ were grown using an oxygen-plasma assisted MBE system (DCA MBE M600, Finland) with a base pressure of 2×10^{-10} Torr. The films were grown on (100) oriented MgO (1×1 cm) single-crystalline substrates. The substrates were cleaned by sonication in acetone and isopropanol and then annealed *in-situ* at 600°C for thirty minutes in ultra-high vacuum (UHV) followed by a further two hours in 1.3×10^{-5} Torr oxygen partial pressure. To grow the magnetite thin film layers, an Fe flux was produced by e-beam evaporating from metallic iron (99.99%), which was directed onto the substrate with a very low growth rate (0.08 Å/s), while the films were simultaneously oxidised by molecular oxygen in the chamber. The substrate temperature was kept at 250°C. In contrast to most previous reports on plasma assisted MBE grown Fe_3O_4 the oxygen reactive atmosphere was solely molecular oxygen. The crystalline quality of thicker layers was assessed by XRD, and XRR thickness measurements were used to calibrate growth rates prior growth of the multi-layer structures.

Subsequent to each Fe_3O_4 layer, $MgFe_2O_4$ or MgO layers were grown on top with nominal 2 nm thickness. In order to grow the $MgFe_2O_4$ interlayer, co-deposition was utilised. Material was e-beam evaporated from pure metallic Fe and ceramic MgO in separate sources onto the substrates. Corresponding samples without the inter layers, but with the same total amount of Fe_3O_4 were

also prepared simultaneously by partly shadowing the samples for comparison (B-samples). Gold contacts were patterned *in-situ* using a shadow mask. Finally, an MgO capping layer of approximately 20 nm was grown at a rate of 0.1 Å/s on top of the gold contacts to avoid unwanted oxidization (see Fig. 1). Post growth samples have been cut by a diamond saw to separate the A and B part for further measurements.

To directly image the sample structures, TEM measurements of selected sample cross sections have been performed. The samples were first coated with 5 nm of gold. They were then loaded into a Carl Zeiss Auriga dual beam FIB/SEM equipped with a micro manipulator needle and gas injection system. A 100 nm platinum strap was deposited on the surface by e-beam followed by a further 1 μm with I-beam in order to protect the region during milling. A cross section of the surface was extracted and transferred to a TEM grid. The ion beam was then used to thin the lamella to approximately 60 nm. An FEI Titan operating at 300 kV was used to image the sample in both bright field TEM and HAADF-STEM modes.

The overall sample thickness of capped single layers as well as all multilayers were also analysed by X-ray reflection using a Bruker D8 Advance with monochromised Cu-Kα X-rays. These measurements were used to independently measure total film thickness, as well as confirm the sharpness of the superlattice structures themselves. Details of the XRR-fits and a table of all sample geometries analysed are found in the supplemental material.[24]

Raman measurements were performed with a Renishaw inVia Raman microscope. Polarisation dependent measurements were performed in backscattering geometry with $z(x_{100}, x_{100})\bar{z}$ and $z(x_{100}, y_{010})\bar{z}$ configuration. To improve the elastically scattered background as well as any contributions from the E_g modes of the substrates, the difference between those measurements has been analysed. This way only contributions with A_{1g} symmetry are considered. Both a 488 nm Ar laser and a 532 nm solid state laser have were with an incident power of 10 mW and integration time of 10 min for samples on MgO substrates and 40 min for samples on $SrTiO_3$. The latter measurements required a numerical subtraction of the intense substrate signal prior to further analysis. The detailed procedure is outlined in the supplemental material.[24] The Raman line shape was analysed by least square fitting of a Voigt profile. The total full width half maximum and peak position were analysed.

The resistivity of each film was measured as a function of temperature (300 K to 75 K) in a linear four point probe geometry using the gold contact patches deposited *in-situ* prior to MgO capping. The magnetic hysteresis loops of the films were measured using a Quantum Design physical properties measurements system (PPMS). The PPMS is equipped with a vibrating sample magnetometer (VSM) with a sensitivity of 5×10^{-7} emu which was used to measure the saturation magnetization.
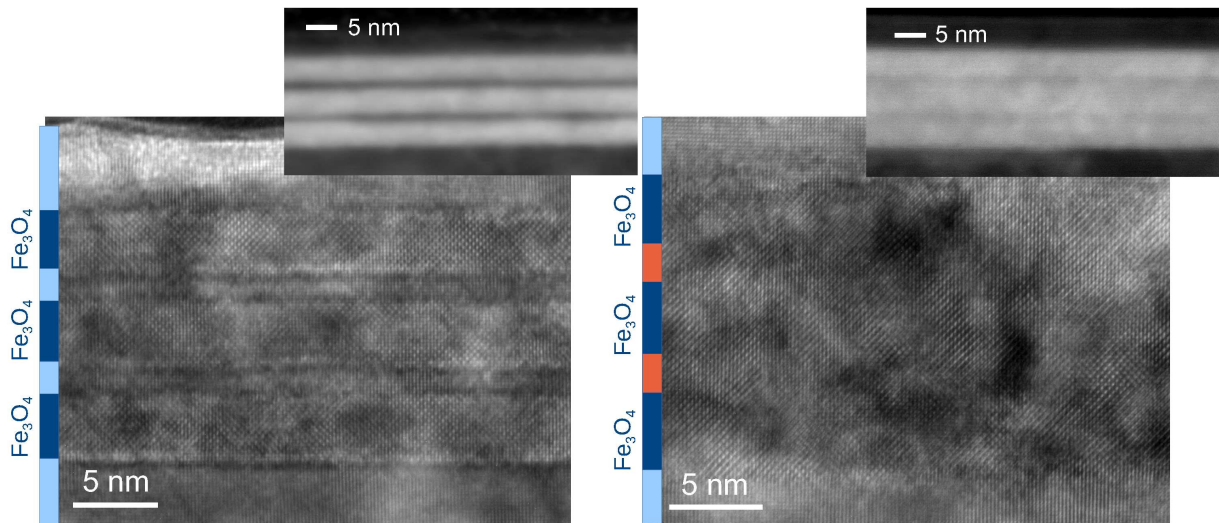
FIG. 2. TEM micrographs of multilayered samples. The left panel shows a sample with 4 nm Fe_3O_4 layers using 2 nm MgO spacers, the right panel shows a sample with 1.5 nm $MgFe_2O_4$ spacers. The insets are taken in HAADF mode where the Z-contrast between the Fe_3O_4 and MgO is apparent. The $Fe_3O_4/MgFe_2O_4$ sample shows less contrast as there is still significant amounts of iron in the spacer. Likewise the different crystal structure of the MgO spacer is clearly seen, while the similarity between the Fe_3O_4 and $MgFe_2O_4$ crystal structures makes it difficult to observe the layering by TEM.

II. RESULTS

Sample structure

Selected multilayers were analysed by TEM to confirm the nominal sample geometry and assess potential problems of e.g. Mg interdiffusion. Figure 2 shows TEM images of two multilayer samples with three Fe_3O_4 layers (nominal thickness 4 nm), spaced by MgO and $MgFe_2O_4$ (nominal thickness 2 nm) respectively. In the sample with MgO spacers, the individual layers can be clearly distinguished by the difference in the lattice structure of MgO and Fe_3O_4. For the sample with $MgFe_2O_4$ spacers, only indirect confirmation on the layering can be seen, as the bright field image is dominated by the positions of the oxygen atoms. As the latter do not differ in position or density between $MgFe_2O_4$ and Fe_3O_4 there is no contrast between spacer and Fe_3O_4 layers.

In high angle annular dark field (HAADF) scanning TEM (STEM) images (Fig. 2 insets), which is more sensitive to Z-contrast, the spacer layers can be observed as weak darker bands, due to the reduced Fe content of the $MgFe_2O_4$ spacer. In addition the total sample thickness between the MgO substrate and MgO capping layer is consistent with the nominal sample geometry as indicated schematically in Fig. 2.

Due to the identical symmetry of the $MgFe_2O_4$ and Fe_3O_4 oxygen sub-lattice we could not confirm sharp interfaces in multilayers with $MgFe_2O_4$ spacers. To confirm the presence of defined $MgFe_2O_4$ layers, as well as for independent thickness confirmation all samples have been analysed by XRR, and measured data have been fitted
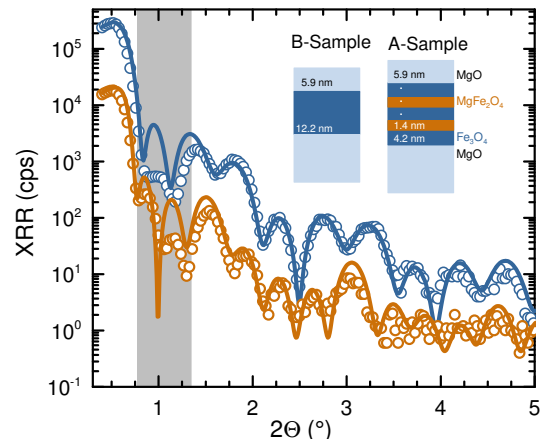

FIG. 3. The raw data of the XRR measurements and the least square fits for a sample with and without $MgFe_2O_4$ spacers. The XRR measurements differ due to the different total film thickness, and difference in internal structure. The data for the multilayered sample have been divided by 10 for better visualisation. The area marked in grey is dominated by instrumental, systematic errors from a non-ideal primary X-ray beam and residual Au contacts.

to extract total and individual layer thickness. Figure 3 shows the result for the sample analysed by TEM for the multi-layered part and the single layer reference part A. The data show a clear difference between the single and multilayer part and the data are consistent with the fits assuming a perfect periodic multilayer with sharp interfaces. Thickness values extracted from the XRR measurements have been used to calculate the Fe_3O_4 resis-
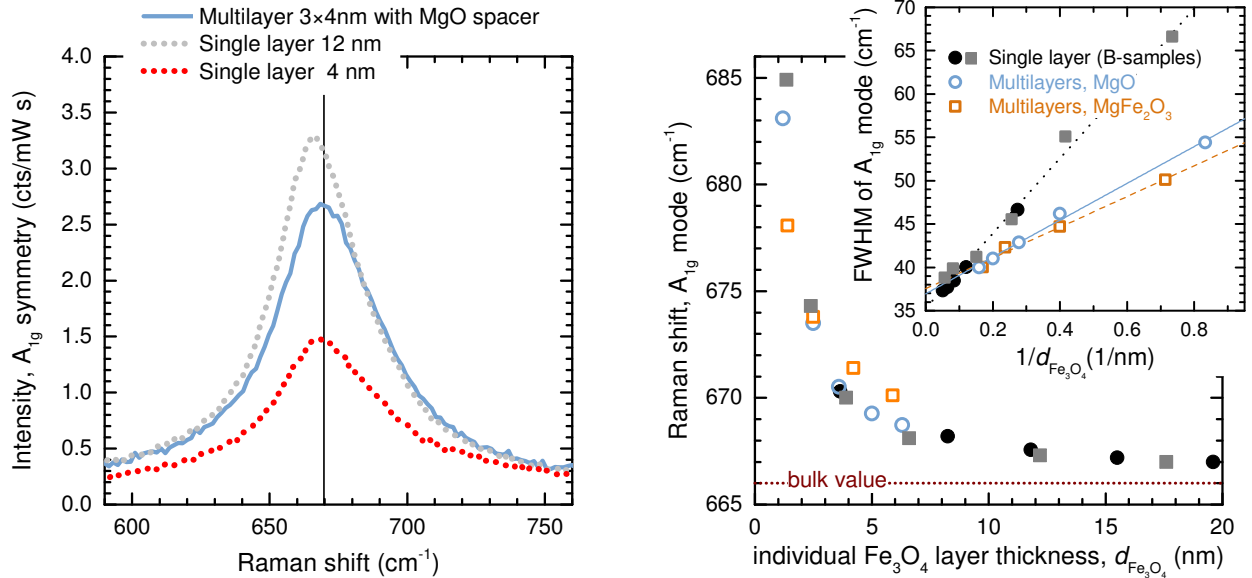
FIG. 4. The Raman spectra (a) reveal distinct size related shifts in the Fe_3O_4 A_{1g} mode. The vertical line indicates the centre of the peak in the multilayer sample which is aligned with that of the single 4 nm layer sample. The continuous 12 nm thick B-sample shows a Raman shift closer to the bulk value. (b) shows the fitted peak position of all samples as a function of the individual Fe_3O_4 layer thickness. The inset shows the width of the mode versus reciprocal individual layer thickness. The peak width of an oxygen breathing mode should strongly depend on the oxygen stoichiometry linking the distinctly different behaviour for single and multilayered samples (closed and open symbols respectively) to an altered stoichiometry. APBs have also been linked to an increased FWHM and their reduction can explain the difference between the samples with $MgFe_2O_4$ and MgO spacers (open squares and circles respectively)

tivity and magnetisation subsequently. A full description of the fitting procedure and complete list of samples and their nominal and measured geometry is found in the supplement.[24]

Typically the measured thickness was within 10% of the nominal thickness. Deviations between nominal, and XRR-fitted thickness for parts A and B have also been used to estimate the magnitude of the thickness error, dominating the error of the magnetisation measurements for ultra-thin films. For samples where TEM images were available, no deviation from the expected thickness and the one seen in TEM were found.

For ultra-thin films XRD measurements are not suitable to analyse the crystalline quality. Alternatively Raman spectroscopy was used here to assess the Fe_3O_4 crystalline quality and via analysis of size effects in the Raman shift also to indirectly confirm sharp interfaces in samples with $MgFe_2O_4$ interlayers.

Of particular focus was the A_{1g} mode of Fe_3O_4 around $668\,cm^{-1}$. The mode position, width and shape is known to be sensitive to the crystalline quality[25,26], strain[27,28], number of APBs[29,30], as well as the oxidisation state.[26,31] In addition, for ultra-thin layers we expect a size dependence similar to what is seen for Fe_3O_4 nano-particles.[32] Figure 4(a) shows the set of spectra from 4 and 12 nm single layers, and a layered sample of 3×4 nm Fe_3O_4 with 1.5 nm $MgFe_2O_4$ spacer layers. The measured Raman intensity scales with the scattering volume, as the penetration depth of the Raman laser is well above the actual

film thickness. The peak position for the single 3 nm layer is shifted to higher wave numbers compared to the 12 nm thick sample. The peak position for the multilayer sample is found to be identical to that of the 4 nm sample, confirming that the Fe_3O_4 layers are well separated individual layers. Figure 4(b) shows the peak position for the complete sample set as a function of individual layer thickness ($d_{Fe_3O_4}$), illustrating that the latter determines the A_{1g} peak position in our high quality Fe_3O_4 samples. Strain effects on the energetic position of the Raman mode can be excluded as all films are equally strained, fully confined to the substrate lattice. Equally no asymmetry, which would indicate over-oxidation and consequent γ-Fe_2O_3 formation[21], is seen in the Raman modes of the capped samples.

While the peak position is mostly affected by the individual layer thickness, independent of number of layers or type of spacer layer, the peak width is found to be significantly different between single and multilayer samples. The A_{1g} mode was found to be more symmetric and sharper for either thicker layers, or samples employing the spacer layers, in particular if $MgFe_2O_4$ spacer layers are used. The Raman data hence not only confirm the expected layering in the samples, but also highlight that by employing a multilayer with similar individual Fe_3O_4 thickness, the signal to noise is significantly improved in the measurement when compared to a single layer due to the increased volume of the sample. They also confirm that by replacing the MgO spacers with $MgFe_2O_4$ spac-

ers, the film quality further improves while maintaining the integrity of the layer confinement, thus such samples can be used to investigate the enhancement of the magnetic moment as we can now separate size effects from other changes such as the number of APBs, as well as improving the SNR by tripling the amount of material in the measurement.

We have to stress that all thin films, multi- or single layers will be epitaxially fully strained with an in-plane lattice constant of $2 \times a_{MgO}$. The lattice mismatch between $MgFe_2O_4$ and Fe_3O_4 or MgO is even lower than that of Fe_3O_4 and MgO. Hence even films up to $100\,nm$ will be fully strained.[33] Hence the A_{1g} peak position itself is initially offset from bulk values due to the strain within the film. For $d_{Fe_3O_4} < 5\,nm$ an additional blue shift is observed. The origin of the latter can not be attributed to a single cause, as multiple effects can result in such a shift. One possibility would be Mg diffusion. The corresponding A_{1g} mode of $MgFe_2O_4$ is found at higher frequencies ($707\,cm^{-1}$).[34] To explain the magnitude of the shift by formation of $Mg_xFe_{1-x}O_4$, we would need Mg concentrations x of 0.08 to 0.19 for the $6\,nm$ and $3\,nm$ samples respectively, assuming a linear dependence on mode position and x. The obtained values for x are inconsistent with the resistance and magnetoresistance data from the same films, as a significant reduction in conductivity and increase in magneto resistance is expected for Mg doped Fe_3O_4.[35] In addition the position is found to equally shift to higher wavenumbers for multilayers with MgO and $MgFe_2O_4$ spacers, and for single layers on $SrTiO_3$ and GaAs.[27] In the latter two cases there is no source of Mg. It is hence more likely that the observed peak shift is directly related to the size reduction. For Fe_3O_4 hollow spheres, a blue shift in the A_{1g} mode has been observed with decreasing diameter and wall thickness.[32] A direct comparison with smaller Fe_3O_4 nanoparticles is difficult due to the large differences in the stoichiometry between chemically synthesised nanoparticles and high quality epitaxial thin films. The effect of dimensional confinement on Raman spectra is well studied for silicon, where in porous silicon the size can be independently controlled by the crystallinty, but also for many oxide nanoparticles.[36] In the case of Fe_3O_4 in particular, no systematic study of the Raman size effect has been performed yet. While first order Raman spectroscopy typically only probes the Brillioun zone centre (Γ-point), the size reduction in the probed sample can lead to a non negligible momentum transfer of the incident photon, resulting in an effective averaging of phonon modes with non-zero momentum in the Raman measurement.[36] Depending on the phonon dispersion of the mode under investigation, this can either lead to a blue shift (minimum at the Γ-point) or red shift (maximum at the Γ-point). The phonon dispersion of Fe_3O_4 has been previously investigated, but particular focus was on the low energy phonon modes, believed to be of importance for the Verwey transition.[9,37,38] Calculated phonon dispersions including the higher energy modes show both modes with maxima and minima in the energy region of interest.[39] Unfortunately they have not been assigned to individual modes at the zone centre to verify our explanation. In case the observed shift with decreasing film thickness is caused by such a Raman size effect, rather than changes in the stoichiometry or crystalline order of the thin film an increase in line width is also expected, consistent with our measurements. The inset in Fig. 4 includes linear fits of the observed line width with reciprocal layer thickness. For all cases the expected linear behaviour is observed. The Raman size effect is significantly less pronounced than for nanoparticles, as our films are only confined in one dimensions. Compared to e.g. CeO_2 nanoparticles[36] where the corresponding slope of the $466\,cm^{-1}$ mode was found to be $125\,cm^{-1}nm$, we observe 43, 21, $18\,cm^{-1}nm$ for Fe_3O_4 single layers, multilayer with MgO and $MgFe_2O_4$ spacer respectively. We have to highlight already a stark difference in the slope between multilayer and single layer samples, which will be discussed at a later stage.

Even with the evidence for the Raman size effect, other possibilities need to be addressed: The charge and crystallographic reordering at the Verwey transition is known to cause a blue shift of the A_{1g} mode itself.[40] It is possible that the Fe_3O_4 thin film does not undergo the Verwey transition, but remains in the low conducting charge ordered phase. However, the Raman line width is dramatically increased in our case and the Verwey transition temperature is typically reduced, the thinner the film. Finally the shifts are most prominent for the thinnest films. It is therefore also possible that we observe evidence of quantum confinement affecting the electronic properties, which due to strong electron-phonon coupling in Fe_3O_4 alters the vibrational states.

In summary, we have to stress that whatever the cause of the changed energetic position of the A_{1g} mode, it is maintained in the multilayered samples and can be used to confirm that the size confinement in the multilayers is fundamentally the same as in single layers. This is of particular use in the samples with $MgFe_2O_4$ spacers, where TEM images only show poor contrast between the two materials. The Raman analysis provides evidence in that case, that there is little intermixing and the Fe_3O_4 layers are well separated from the $MgFe_2O_4$ layers. Secondly the Raman line width for samples as thin as $6\,nm$ in the case of multilayers and $12\,nm$ in the case of single layers is already as low as typically found in bulk films ($35\text{-}40\,cm^{-1}$). This is direct evidence of a very high crystalline quality in all our Fe_3O_4 films.

Resistance and magneto resistance

Electrical measurements (Fig. 5) on the B-Samples show very good conductivity ($6\,m\Omega cm$ at $300\,K$) and most importantly a sharp Verwey transition at $113.2\pm0.5\,K$ for $15\,nm$ thick layers. Even in $8\,nm$ thick samples a Verwey transition at $107.7\pm0.5\,K$ can be ob-
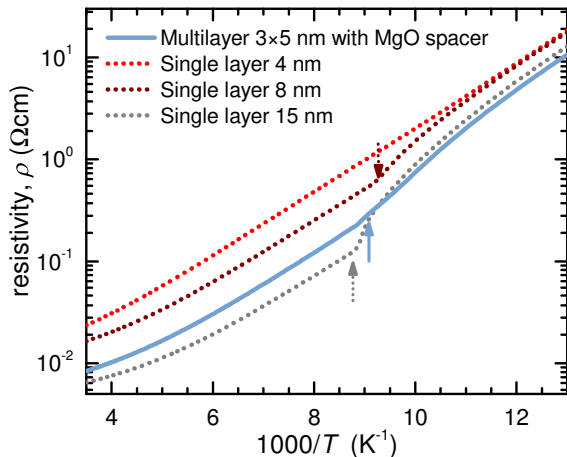
FIG. 5. Verwey transition in thin films: Resistivity of B-samples with thickness of 15, 8, and 4 nm (dotted lines). For the 15 nm and the 8 nm samples, the Verwey transition is clearly observed as indicated by the arrows. In comparison an A-sample (3×5 nm Fe_3O_4 with 2 nm MgO, solid line) with 5 nm individual Fe_3O_4 thickness is also shown. The improved layer quality in this case already leads to a lower resistivity than seen in a 8 nm single layer, with the Verwey transition still occurring. However there is a size induced reduction in the resistivity and shift in he Verwey transition compared to the corresponding B-sample ($d_{Fe_3O_4}$ =15 nm). All films have been grown on MgO(001)

FIG. 6. Magneto resistance at 300 K of a set of samples with 4 nm thick Fe_3O_4 layers, either as single layer (red, dotted line), as three layers spaced with 2 nm MgO (blue, solid line) or with 1.5 nm $MgFe_2O_4$ (orange, dashed line). All films have been grown on MgO(001)

served, confirming the very high quality of the Fe_3O_4 ultra thin layers, once they are protected from further *ex-situ* oxidisation in air. In A-samples with $MgFe_2O_4$ and MgO spacer layers the resistivity increases if compared to their corresponding continuous B-Samples. However if one compares the resistivity of multilayered samples with continuous layers of similar individual layer thickness, the resistivity in the multilayered samples is significantly reduced. One such example is shown in Fig. 5. Remarkably, even in samples with 5 nm individual layer thickness the Verwey transition can be observed. These results significantly lower the previously reported Fe_3O_4 minimum thickness at which the transition is observed and give a first indication that the multilayered ultra-thin films have a better crystalline quality than single layers of the same thickness.

In epitaxial thin films the presence of anti-phase boundaries (APBs) is known to affect the resistivity of the films, but more importantly their magneto-resistance.[15,41–43] The formation of the APBs is of particular importance in samples grown on MgO(001), where single height steps can increase their number significantly.[42,44–46] To investigate how the formation of APBs is altered in our multilayers we performed magneto-resistance measurements exemplary shown in Fig. 6. The sample with $MgFe_2O_4$ spacer layers shows reduced MR compared to either one with MgO spacers or a single 4 nm thick layer. It was previously confirmed that
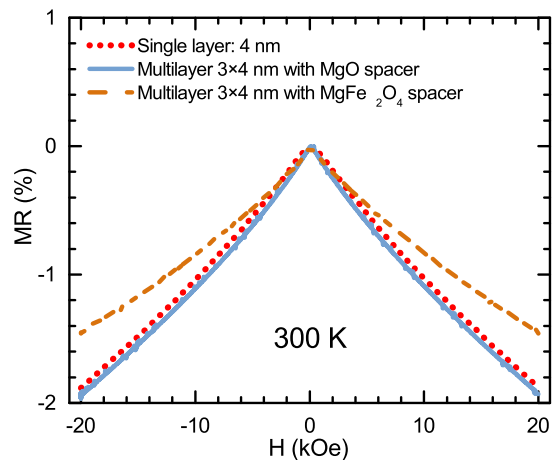
the number of APBs decreases, the thicker the Fe_3O_4 layer.[15,41] By introducing a spacer layer of similar lattice geometry to Fe_3O_4 itself, e.g. spinel $MgFe_2O_4$ or $MgAl_2O_4$, the number of APBs in the 2nd and 3rd Fe_3O_4 layer are effectively reduced. The multilayer concept therefore allows the decoupling of size effects from the density of APBs for samples grown on the same substrate. Indeed the measured MR in the Fe_3O_4/$MgFe_2O_4$ multilayer on an MgO substrate is already lower than that reported for 10 nm Fe_3O_4 on $MgAl_2O_4$ symmetry matched substrates, where APBs are only formed due to misfit dislocations due to the higher lattice mismatch.[47–49] The MR data already suggests that in the case of MgO spacer layers, the natural roughness of the MgO spacer prevents the reduction in APBs with thickness, and might even lead to an increase in number. While our measurements can not provide absolute values for the APB densities we can estimate the relative change in densities. Assuming the MR is solely caused by APBs and proportional to the APB density, the 3×4 nm sample using 1.5 nm $MgFe_2O_4$ spacers already has a 30% lower APB density compared to the corresponding single layer of sample with MgO spacers. As only the 2nd and 3rd Fe_3O_4 layer will be actually different from a single layer, this implies the APB density can be reduced by the same amount in a single Fe_3O_4 layer if a 5 nm $MgFe_2O_4$ buffer layer would be used.

Magnetic moment

After confirming that the multilayer structure preserves the size confinement in Fe_3O_4 layers, and that by employing $MgFe_2O_4$ spacer layers the density of APBs can be reduced compared to single layers of similar in-
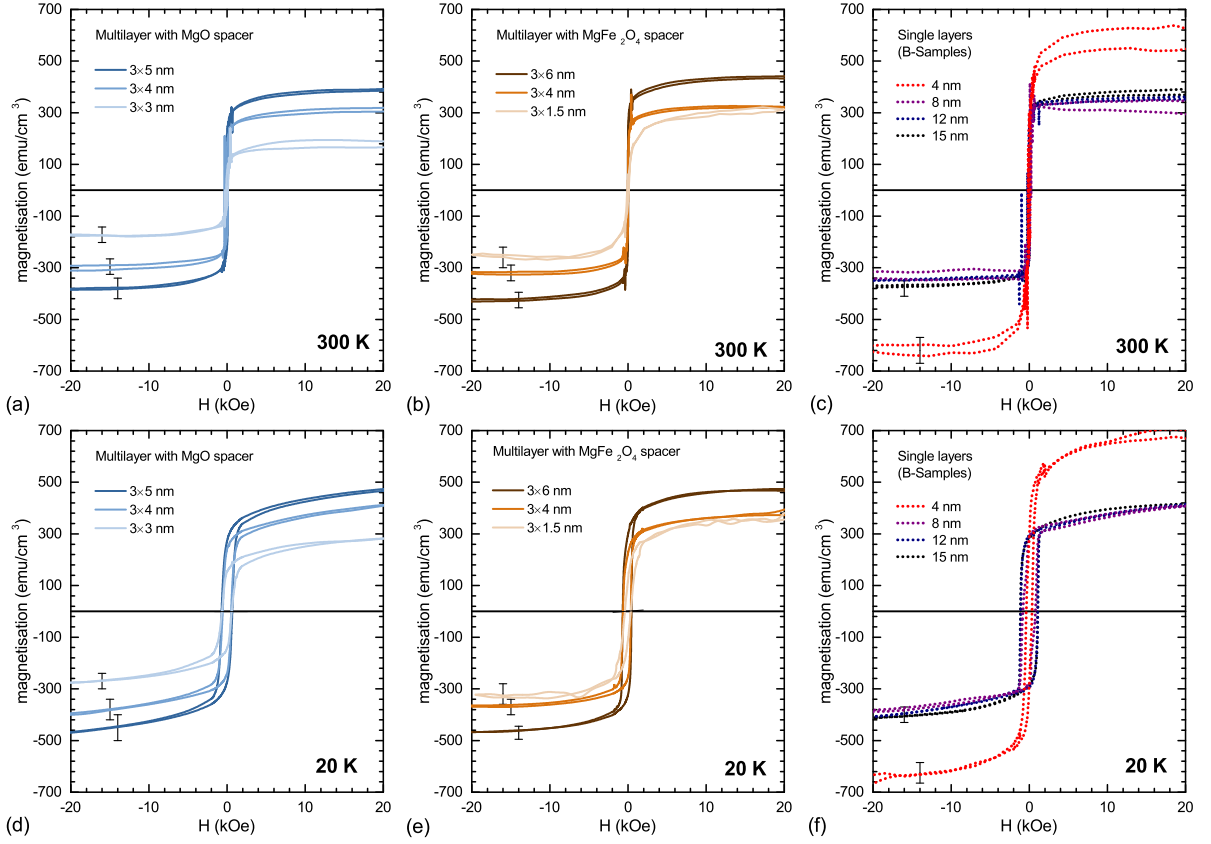
FIG. 7. Measurements of the magnetic moments of multi- and single layered samples at 300 K (top row) and 20 K (bottom row). An increased magnetic moment was only observed for single layered films with $d<5$ nm.

dividual Fe_3O_4 layer thickness, we are now able to investigate if the Fe_3O_4 thin films do show an enhanced magnetic moment. Due to the increased total volume of thin film by employing multilayers, systematic errors in thin film magnetic measurements (due to e.g. small contributions from para- or ferro-magnetic impurities in the substrate) are significantly reduced. Equally the re-optimised growth conditions produced high quality thin films, where the crystalline structure is not only stoichiometric, confirmed by the Raman line width close to those of bulk samples, but also the Fe_3O_4 characteristic Verwey transition is observed even for $\sim$5 nm thin films. Figure 7 shows the results magnetic moment measurements of the multi layered and single layer Fe_3O_4 films. While in the single layers we observe the increased magnetic moment for the thinnest sample, the finding is not confirmed in the multi layers which have better SNR. On the contrary, the magnetic moment is reduced for both samples with a high density of APBs (MgO spacer) and those with better magnetic domain ordering ($MgFe_2O_4$ spacer).

III. DISCUSSION

Our results so far confirm that the increased magnetic moment does not originate from an inherent size effect as it is not observed for the multilayer samples. Due to the very high crystalline quality of the samples, as confirmed by the presence of the Verwey transition and the closeness of the A_{1g} Raman mode peak width to bulk values, we can also exclude that structural defects affected the measurements. This also excludes the possibility that interface states have the effect of contributing to the enhanced moment, as the number of interfaces in our multilayers is increased. Any interface effect would consequently also scale in proportion to the number of layers.

This leaves only the direct influence of the substrates on the measurements. It has been previously suggested that Fe or other magnetic impurities affect the results.[19] Despite our best efforts we could not detect any magnetic signal from plain substrates at room temperature, where the increased moment was also seen in the single layer samples. We therefore suggest another mechanism, supported by our results. One of our key findings is that the single Fe_3O_4 films show an increased line width in the A_{1g} Raman mode compared to its multilayered counterparts as evident by a much steeper slope in the FWHM vs. inverse film thickness plots (see Fig. 4). Both, size effects and the number of APBs can affect the Raman line width, but both the size confinement and number of APBs are expected to be similar for the single Fe_3O_4 on MgO layer

and the triple layer with MgO spacers. The contributions of APBs to the FWHM is much smaller as evident by the small difference in the FWHM between MgO and $MgFe_2O_4$ spacers, even though their APB density significantly differs as seen in MR data (see Fig. 6). The significantly broader mode of the single layer, and larger slope in the width vs. reciprocal layer thickness analysis must hence originate from increased stoichiometric disorder. The A_{1g} mode around $670 \, cm^{-1}$ only involves movement of oxygen atoms,[37,39,50] suggesting that a disordered oxygen sublattice is affecting it most.

Over-oxidisation of Fe_3O_4 e.g. at the surface is known to lead to the formation of γ-Fe_2O_3.[21,22,31] As maghemite has a smaller magnetic moment than Fe_3O_4 an oxygen surplus would lead to a reduction in the magnetic moment. Conversely an under-oxidisation could lead to an increase in the magnetic moment and could be the root cause of the observations. The most likely point defect to lead to an effective under-oxidisation are oxygen vacancies. During the formation of the Fe_3O_4 layers, oxygen can migrate into the substrate, effectively reducing the first layers of the Fe_3O_4 films – providing an under stoichiometric substrate surface. In our multilayers this mechanism will only affect the first layer, but not the subsequent layers separated by stoichiometric spacer layers of MgO or $MgFe_2O_4$. This mechanism can also explain why the effect is not seen universally as substrate quality and preparation conditions between groups varies. In particular the substrate cleaning steps are typically performed by *in-situ* vacuum annealing, which is known to be capable of increase the density of oxygen vacancies.

In many transition metal oxides the creation of oxygen vacancies upon vacuum annealing is well studied.[51] However, few studies explicitly discuss this for MgO, where the effect is more localised to the MgO surface layers.[52,53] We therefore prepared a set of test Fe_3O_4 layers on $SrTiO_3(001)$ substrates, so that the number of bulk oxygen vacancies could be more readily controlled.[54,55] Figure 8 compares the magnetic moment of a 6 nm thin single Fe_3O_4 layer on two different $SrTiO_3$ substrates, one was vacuum annealed at 600°C the other at 800°C. While the one on the low temperature annealed $SrTiO_3$ substrates shows a similar magnetic moment to the films grown on MgO shown above, the sample grown on the high temperature annealed $SrTiO_3$ substrate has a significantly enhanced moment. The high temperature annealing of the $SrTiO_3$ substrates creates a significant quantity of bulk oxygen vacancies[56], clearly verified by discolouration of the substrate (see Supplementary information S5). The presence of these vacancies, in particular at the surface region, leads to the already suspected reduction of the Fe_3O_4 thin film, thus increasing the magnetic moment. The annealing temperature of 600°C and 800°C was carefully chosen, in order to avoid changes in surface morphology and step density seen for higher temperature annealing of STO[57,58], while at the same time altering the concentration of oxygen vacancies.

A line shape analysis of the A_{1g} mode for these films is more complicated on STO grown films due to a strong substrate background signal. The latter was numerically removed as detailed in the supplementary information.[24] Figure 8 shows the mode and a least squares fit for each sample. While the position of the mode is quite similar ($670.1 \pm 0.5 \, cm^{-1}$ and $668.4 \pm 0.7 \, cm^{-1}$) the mode width significantly differs between the sample grown on the 600°C or 800°C annealed substrate ($42.3 \pm 3 \, cm^{-1}$ and $50 \pm 4 \, cm^{-1}$ respectively). This is fully consistent with our model of an altered Fe/O stoichiometry in films directly grown on the substrate with more oxygen vacancies. The A_{1g} mode is very sensitive to the oxygen stoichiometry and disorder, as the probed vibration is a breathing mode of the oxygen octahedra.[37] Over oxidisation in the form of γ-Fe_2O_3 formation could lead equally to a broadening of the mode but is accompanied with a blue shift to higher wave numbers and stark asymmetry in the peak.[21] In contrast we observe a small red shift to lower wave number in addition to the significant broadening, further suggesting a reduction of the film. Interestingly on similarly strained 5 nm Fe_3O_4 thin film with a low number of APBs grown on GaN, no enhanced magnetic moment has been observed.[59] This illustrates that in non-oxide substrates, where by definition oxygen vacancies can not migrate from the substrate, reduction of the Fe_3O_4 thin film can also be prevented.

Our findings suggest, that for ultra-thin Fe_3O_4 films the substrate stoichiometry can thus substantially alter the magnetic properties of the films as oxygen can migrate into the substrate bulk, leaving a Fe_3O_4 film with an increased number of oxygen vacancies. It is evident that the enhanced moment is only seen in films well below 8 nm and only in single layers. While the moment for films in this study is lower than in a previous study on $MgO(100)$[11], the magnitude of the increased moment of a single layer of 4 nm compared to a 8 nm film is confirmed. The wide spread of data points in the inset of Fig. 9 illustrates that the moment of thin film Fe_3O_4 does depend on many parameter such as crystalline quality and APB density. Our data clearly indicate though that the frequently observed increased moment is not inherent to a size effect in high quality Fe_3O_4 but rather linked to an altered oxygen stoichiometry induced by the substrate. The enhancement is therefore not seen for films grown in multi-layers, where the substrate is decoupled from the thin films by the stoichiometric spacer layers. It is equally absent if the substrate itself does not possess a large number of oxygen vacancies, such as seen in films grown on Al_2O_3.[14]

From a phenomenological point of view the specific magnetic moment of several bulk magnetic iron oxides and iron can be compared (see Fig. 9), showing that as a general trend the moment increases with increased iron content. However the magnetisation of off-stoichiometric films will highly depend on the exact nature of the oxygen vacancy or possible defect complexes. One of the few theoretical studies on the impact of oxygen vacancies in Fe_3O_4 found no significant change in the overall mag-
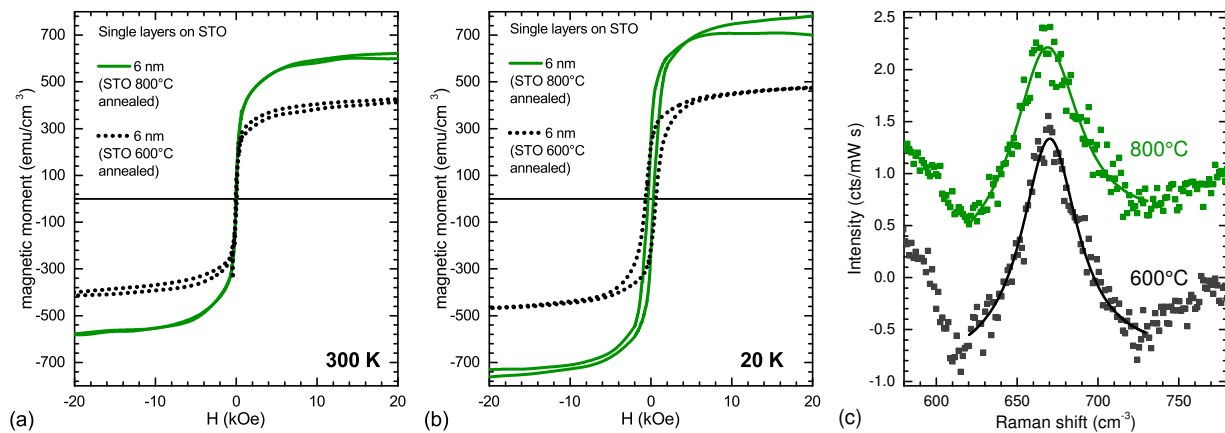
FIG. 8. Magnetic moment for 6 nm thick single layer Fe_3O_4 samples on $SrTiO_3$ measured at 300 K (a) and 20 K (b). The measurements for films grown on two different $SrTiO_3$ substrates are shown, where one was vacuum annealed at 600°C and one at 800°C. (c) shows the A_{1g} Raman mode of the magnetite thin films for the same two samples. The one grown on the substrate annealed at 800°C shows a broader A_{1g} mode associated with a more off-stoichiometric Fe_3O_4 lattice.
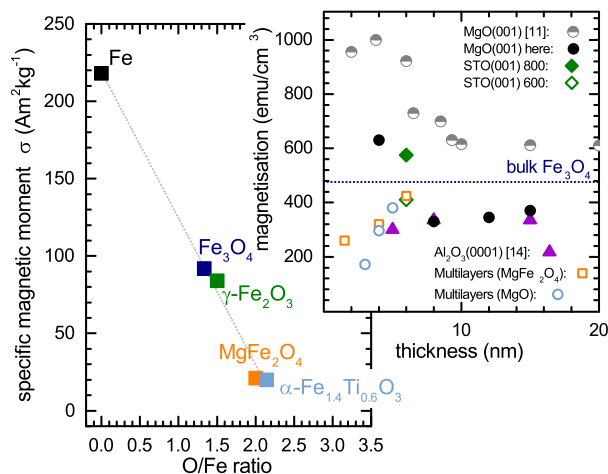

FIG. 9. Specific magnetic moment of bulk materials as a function of oxygen/iron ratio for selected iron oxides in a spinel or closely related lattice. Values for iron are included for comparison. The graph illustrates a general trend in bulk materials of an increased moment in lattices with reduced oxygen content. (data taken from J. M. D. Coey[60]) The inset summarises the dependency of the magnetic moment of Fe_3O_4 thin films investigated here and compared to previous literature data for the growth on MgO and Al_2O_3 surfaces.

netisation, however only isolated single oxygen vacancies (V_O) have been considered.[61] A more recent combined experimental and theoretical study on Fe_3O_4 grown on GaAs(100) concluded that oxygen vacancies do affect the ferrimagnetic coupling between iron on tetrahedral and octahedral sites, explaining the net increase in the magnetic moment.[16] Likewise in thicker Fe_3O_4 films grown by PLD in various oxygen partial pressure conditions, the films grown at the lower p_{O_2} have shown higher magnetisation. That study was performed on Si(001), where

strain affects the magnetic properties and the phase purity of the films was much worse than the MBE grown films investigated here.[62] In related oxides, namely spinel ferrites such as $NiFe_2O_4$ grown on STO, oxygen vacancies have been previously discussed as a root cause for the enhanced magnetic moment, but the effects of the cation disorder of the two inequivalent cations Ni and Fe were concluded to be the more dominant contribution.[63] In binary Fe_3O_4 the latter would be equivalent to an increase in Fe^{+3}-A, Fe^{+3}-B, and Fe^{+2}-B site disorder. Site disorder is more likely in a defective lattice with a high number of oxygen vacancies. Alternatively, there could be a phase separation into stoichiometric Fe_3O_4 in the film and metallic iron or FeO at the substrate/film interface. The possibility of an interface FeO layer has been previously discussed in films grown on MgO(001).[64] However, a paramagnetic FeO layer would not result in an enhanced magnetic moment in such a thin film. We therefore suggest that the oxygen poor interface layer is better described as a Fe_3O_4 layer with a high number of oxygen vacancies, rather than a formation of the paramagnetic wüstite phase. This is consistent with the data of Bertram et al.[64] as their assessment is based on XRR and XPS data, which are sensitive to the density of the interface layer and charge states of Fe, but not necessarily to the crystal structure.

IV. CONCLUSION

By analysing the electric, magnetic and crystallographic properties of ultra-thin Fe_3O_4 films grown on MgO(001), in the form of Fe_3O_4/MgO and Fe_3O_4/$MgFe_2O_4$ super-lattices, we were able to demonstrate that the frequently observed increased magnetic moment is not an inherent property of Fe_3O_4, but related to changes in the Fe_3O_4 stoichiometry on oxide substrates

with high number of oxygen vacancies. Thus we can confirm that the oxygen vacancy mechanism suggested by Huang *et al.*[16] is also responsible for the increase in ultrathin Fe_3O_4 grown on oxide substrates. However the root cause for the oxygen vacancy formation in Fe_3O_4 is a high density of oxygen vacancies in the surface region of the substrate, rather than deposition conditions. Optimising the latter for thick films does not lead to high quality thin films due to these substrate interactions.

Indeed our Fe_3O_4 ulrathin films grown at a reduced growth rate from metallic Fe, and using only molecular oxygen as the oxidising agent, are of high crystalline quality, which was indicated by the presence of the Verwey transition even in films as thin as 6 nm and by the sharp A_{1g} Raman modes.

In super-lattice structures the magnetic moment is reduced in thin films below 6 nm thickness, while in single layers grown directly on the substrate surface the magnetic moment can be increased. The link between the presence of oxygen vacancies in the bulk or at the surface of the substrate and an enhanced magnetic moment in thin films was demonstrated for 5 nm films grown on $SrTiO_3$ substrates, where the density of oxygen vacancies was increased by vacuum annealing of the substrate prior growth.

Secondly we were able to show that the use of $MgFe_2O_4$ spacer layers, reduced the number of APBs, leading to a weaker magneto resistance and sharper A_{1g} Raman modes. This suggests that using $MgFe_2O_4$ as a buffer layer between MgO and Fe_3O_4 can be employed to significantly improve the properties of even single layer Fe_3O_4 as it will not only reduce the APBs but can also limit the diffusion of oxygen vacancies by increasing the separation of the Fe_3O_4 films from potentially oxygen poor substrates. Other oxide buffer layers[65], or metallic layers have already been effective in improving thin film Fe_3O_4 but the similar lattice structure of $MgFe_2O_4$ and Fe_3O_4 should be better suited to reduce the number of APBs, and strain at the same time as acting as an oxygen diffusion barrier.

While we only investigated Fe_3O_4 films, the proposed mechanism of magnetic moment alterations in ultrathin films by oxygen vacancy diffusion is likely to be found in other magnetic oxides. For example similarly enhanced moments have been found for spinel $NiFe_2O_4$ and $NiCo_2O_4$.[63,66,67] Recent studies have shown that the suggested mechanism of a change in cation distribution in such thin film ternary oxides does not consistently explain the increased moment.[66] We therefore suggest that similar to the presented findings for Fe_3O_4 the *substrate stoichiometry* could play an important role in these related spinels.

* mauito@tcd.ie
† fleisck@tcd.ie
[1] J. P. Hong, S. B. Lee, Y. W. Jung, J. H. Lee, K. S. Yoon, K. W. Kim, C. O. Kim, C. H. Lee, and M. H. Jung, Appl. Phys. Lett. **83**, 1590 (2003).
[2] E. Verwey, Nature **144**, 327 (1939).
[3] F. Walz, J Phys.: Condens. Matter **14**, R285 (2002).
[4] V. Antonov, L. Bekenov, and A. Yaresko, Adv. Condens. Matter Phys. **2011**, 298928 (2011).
[5] M. B. Yazdi, K.-Y. Choi, D. Wulferding, P. Lemmens, and L. Alff, New Journal of Physics **15**, 103032 (2013).
[6] M. S. Senn, J. P. Wright, and J. P. Attfield, Nature **481**, 173 (2012).
[7] S. De Jong, R. Kukreja, C. Trabant, N. Pontius, C. Chang, T. Kachel, M. Beye, F. Sorgenfrei, C. Back, B. Bräuer, et al., Nat. Mater. **12**, 882 (2013).
[8] T. Kołodziej, A. Kozłowski, P. Piekarz, W. Tabiś, Z. Kąkol, M. Zając, Z. Tarnawski, J. M. Honig, A. M. Oleś, and K. Parlinski, Phys. Rev. B **85**, 104301 (2012).
[9] P. Piekarz, K. Parlinski, and A. M. Oleś, Phys. Rev. B **76**, 165124 (2007).
[10] J. Anderson, M. Kuhn, U. Diebold, K. Shaw, P. Stoyanov, and D. Lind, Phys Rev B **56**, 9902 (1997).
[11] S. K. Arora, H.-C. Wu, R. J. Choudhary, I. V. Shvets, O. N. Mryasov, H. Yao, and W. Y. Ching, Phys. Rev. B **77**, 134443 (2008).
[12] Y. Lu, J. Claydon, Y. Xu, D. Schofield, and S. Thompson, J. Appl. Phys. **95**, 7228 (2004).
[13] F. Schedin, E. Hill, G. Van der Laan, and G. Thornton, J. Appl. Phys. **96**, 1165 (2004).
[14] J.-B. Moussy, S. Gota, A. Bataille, M.-J. Guittet, M. Gautier-Soyer, F. Delille, B. Dieny, F. Ott, T. D. Doan, P. Warin, P. Bayle-Guillemaud, C. Gatel, and E. Snoeck, Phys. Rev. B **70**, 174448 (2004).
[15] I. Bernal-Villamil and S. Gallego, J. Phys.: Condens. Matter **27**, 293202 (2015).
[16] Z. Huang, Q. Chen, Y. Zhai, J. Wang, Y. Xu, and B. Wang, Appl. Phys. Lett. **106**, 182401 (2015).
[17] P. Li, C. Xia, Z. Zhu, Y. Wen, Q. Zhang, H. N. Alshareef, and X.-X. Zhang, Adv. Funct. Mater. **26**, 5679 (2016).
[18] Z. Huang, Y. Zhai, Y. Lu, G. Li, P. Wong, Y. Xu, Y. Xu, and H. Zhai, Appl. Phys. Lett. **92**, 113105 (2008).
[19] J. Orna, P. A. Algarabel, L. Morellón, J. Pardo, J. de Teresa, R. L. Antón, F. Bartolomé, L. García, J. Bartolomé, J. Cezar, et al., Phys. Rev. B **81**, 144420 (2010).
[20] F. Voogt, T. Palstra, L. Niesen, O. Rogojanu, M. James, and T. Hibma, Phys. Rev. B **57**, R8107 (1998).
[21] K. Fleischer, O. Mauit, and I. Shvets, Appl. Phys. Lett.

104, 192401 (2014).

[22] F. Bourgeois, P. Gergaud, H. Renevier, C. Leclere, and G. Feuillet, J. Appl. Phys. **113**, 013510 (2013), and references therein.

[23] X. Liu, A. Rata, C. Chang, A. Komarek, and L. Tjeng, Phys. Rev. B **90**, 125142 (2014).

[24] See Supplemental Material at [URL will be inserted by publisher] for details on XRR measurements, FEM simulation on carrier distribution, additional resistivity data, Raman signal extraction for films on STO, STO surface stoichiometry and full list of all sample geometries analysed.

[25] O. N. Shebanova and P. Lazor, J. Solid State Chem. **174**, 424 (2003).

[26] A. M. Jubb and H. C. Allen, ACS Applied Materials & Interfaces **2**, 2804 (2010).

[27] J. Zhang, P. Tan, W. Zhao, J. Lu, and J. Zhao, J. Raman Spectrosc. **42**, 1388 (2011).

[28] Y. Chen, J. Sun, Y. Han, X. Xie, J. Shen, C. Rong, S. He, and B. Shen, J. Appl. Phys. **103**, 7D703 (2008).

[29] D. Phase, S. Tiwari, R. Prakash, A. Dubey, V. Sathe, and R. Choudhary, J. Appl. Phys. **100**, 123703 (2006).

[30] S. Tiwari, D. M. Phase, and R. J. Choudhary, Appl. Phys. Lett. **93**, 234108 (2008).

[31] D. De Faria, S. Venâncio Silva, and M. De Oliveira, J. Raman Spectrosc. **28**, 873 (1997).

[32] M. Francisco, C. Teresa, C. María, P. Ramón, R. Rolando, F. Pedro, S. José María, E. Eduardo, and M. Carmen, Soft Nanoscience Letters **2011** (2011).

[33] O. Mauit, K. Fleischer, B. O'Dowd, D. Mullarkey, and I. Shvets, Thin Solid Films **612**, 290 (2016).

[34] V. D'Ippolito, G. B. Andreozzi, D. Bersani, and P. P. Lottici, J. Raman Spectrosc. **46**, 1255 (2015).

[35] C. Lie, P. Kuo, A. Sun, C. Chou, S. Chen, I. Chang, T. Wu, and J. Chen, Magnetics, IEEE Transactions on **39**, 2800 (2003).

[36] G. Gouadec and P. Colomban, Prog. Cryst. Growth Charact. Mater. **53**, 1 (2007), and references therein.

[37] I. Chamritski and G. Burns, J. Phys. Chem. B **109**, 4965 (2005).

[38] M. Hoesch, P. Piekarz, A. Bosak, M. Le Tacon, M. Krisch, A. Kozłowski, A. M. Oleś, and K. Parlinski, Phys. Rev. Lett. **110**, 207204 (2013).

[39] B. Handke, A. Kozłowski, K. Parliński, J. Przewoźnik, T. Ślęzak, A. Chumakov, L. Niesen, Z. Kąkol, and J. Korecki, Phys. Rev. B **71**, 144301 (2005).

[40] L. Gasparov, D. Tanner, D. Romero, H. Berger, G. Margaritondo, and L. Forro, Phys. Rev. B **62**, 7939 (2000).

[41] S. Celotto, W. Eerenstein, and T. Hibma, EPJ B **36**, 271 (2003).

[42] T. Hibma, F. Voogt, L. Niesen, P. Van der Heijden, W. De Jonge, J. Donkers, and P. Van der Zaag, J. Appl. Phys. **85**, 5291 (1999).

[43] A. Kumar, D. K. Pandya, and S. Chaudhary, J. Appl. Phys. **112**, 073909 (2012).

[44] L. McGuigan, R. C. Barklie, R. G. S. Sofin, S. K. Arora, and I. V. Shvets, Phys. Rev. B **77**, 174424 (2008).

[45] C. Magen, E. Snoeck, U. Lüders, and J. Bobo, J. Appl. Phys. **104**, 013913 (2008).

[46] R. Sofin, S. Arora, and I. Shvets, J. Magn. Magn. Mater. **316**, e969 (2007).

[47] M. Luysberg, R. Sofin, S. Arora, and I. Shvets, Phys. Rev. B **80**, 024111 (2009).

[48] D. Gilks, L. Lari, Z. Cai, O. Cespedes, A. Gerber, S. Thompson, K. Ziemer, and V. Lazarov, J. Appl. Phys. **113**, 17B107 (2013).

[49] W. Eerenstein, L. Kalev, L. Niesen, T. Palstra, and T. Hibma, J. Magn. Magn. Mater. **258**, 73 (2003).

[50] A. D. Rowan, C. H. Patterson, and L. Gasparov, Phys. Rev. B **79**, 205103 (2009).

[51] M. V. Ganduglia-Pirovano, A. Hofmann, and J. Sauer, Surf. Sci. Rep. **62**, 219 (2007).

[52] S. Imad-Uddin Ahmed, S. S. Perry, and O. El-Bjeirami, J Phys. Chem. B **104**, 3343 (2000).

[53] G. Pacchioni, ChemPhysChem. **4**, 1041 (2003).

[54] I. Raevski, S. Maksimov, A. Fisenko, S. Prosandeyev, I. Osipenko, and P. Tarasenko, J. Phys.: Condens. Matter **10**, 8015 (1998).

[55] M. S. M. González, M. H. Aguirre, E. Morán, M. Á. Alario-Franco, V. Perez-Dieste, J. Avila, and M. C. Asensio, Solid State Sci. **2**, 519 (2000).

[56] D. Schwarz and H. Anderson, J. Electrochem. Soc. **122**, 707 (1975).

[57] O. E. Dagdeviren, G. H. Simon, K. Zou, F. J. Walker, C. Ahn, E. I. Altman, and U. D. Schwarz, Phys. Rev. B **93**, 195303 (2016).

[58] K. Szot and W. Speier, Phys. Rev. B **60**, 5909 (1999).

[59] P. K. J. Wong, W. Zhang, X. Cui, Y. Xu, J. Wu, Z. Tao, X. Li, Z. Xie, R. Zhang, and G. Van Der Laan, Phys. Rev. B **81**, 035419 (2010).

[60] J. M. Coey, *Magnetism and magnetic materials* (Cambridge University Press, 2010).

[61] R. Arras, L. Calmels, and B. Warot-Fonrose, Appl. Phys. Lett. **100**, 032403 (2012).

[62] K. Dey, A. Ghosh, P. Modak, A. Indra, S. Majumdar, and S. Giri, Appl. Phys. Lett. **105**, 142905 (2014).

[63] U. Lüders, M. Bibes, J.-F. Bobo, M. Cantoni, R. Bertacco, and J. Fontcuberta, Phys. Rev. B **71**, 134419 (2005).

[64] F. Bertram, C. Deiter, O. Hoefert, T. Schemme, F. Timmer, M. Suendorf, B. Zimmermann, and J. Wollschläger, J. Phys. D: Appl. Phys. **45**, 395302 (2012).

[65] K. Kuepper, O. Kuschel, N. Pathé, T. Schemme, J. Schmalhorst, A. Thomas, E. Arenholz, M. Gorgoi, R. Ovsyannikov, S. Bartkowski, *et al.*, Phys. Rev. B **94**, 024401 (2016).

[66] M. Hoppe, S. Döring, M. Gorgoi, S. Cramm, and M. Müller, Phys. Rev. B **91**, 054418 (2015).

[67] P. Silwal, L. Miao, J. Hu, L. Spinu, D. H. Kim, and D. Talbayev, J. Appl. Phys. **114**, 103704 (2013).

Ultrathin Magnetite in Fe_3O_4/MgO super-lattices – investigating the origin of an enhanced, thin film magnetic moment

Ozhet Mauit, Karsten Fleischer, Cormac Ó Coileáin,
Brendan Bulfin, Daniel S. Fox, Christopher M. Smith,
Daragh Mullarkey, Gulnar Sugurbekova,
Hongzhou Zhang, and Igor V. Shvets

## SUPPLEMENTARY INFORMATION

S1.   Thickness determination

One of the key issues in assessing the magnetic moment and the resistivity of ultrathin oxide layers is the exact knowledge of the layer thickness as it directly affects the derived magnetisation and resistivity values. This is particularly problematic for ultrathin films, where the actual layer thickness can not be directly measured by X-Ray reflection. For our sample set the thickness was initially estimated based on the growth time. The growth rate was was frequently tested by growing thicker reference samples, and the tooling factor of the quartz crystal balance adjusted according to the differences between nominal and actual film thickness measured by XRR. For the individual super-lattices we can measure the total layer thickness, including the capping MgO, as it is always in the range where XRR measurements are possible. The measurements are nevertheless more sensitive to the overall thickness and periodic structure rather then the individual layer thickness. Hence the following routine was used to determine the average layer thickness of the Fe_3O_4 layers within the superlattice.

1. The B-sample, containing the continuous Fe_3O_4 film and MgO capping layer was measured by XRR and the thickness of both layers was fitted.

2. The layered A-sample was also measured by XRR. The measurement was fitted according to an ideal superlattice structure, where the starting parameters ($d_{1/3}$) of the fit were set to be 1/3 of the B-layer thickness for the Fe_3O_4 layers and to the nominal MgO thickness (2 nm) for the spacer layers. The final capping layer thickness was kept fixed to the measured value from the A-sample. Only the thickness of the Fe_3O_4 layer and spacer layer were left as free parameter in the fits.

3. The fitted individual Fe_3O_4 layer thickness was used in the derivation of magnetisation and resistivity, with the error being estimated from the variation of this value from the nominal and $d_{1/3}$.

An example of the analysis is shown in the main article Fig. 3. Data and least square fits are shown for the same sample with $MgFe_2O_4$ spacers, where TEM analysis was available. While in the TEM the contrast between Fe_3O_4 and $MgFe_2O_4$ was not clear, the XRR data confirm the presence of a multilayer by the appearance of superlattice peaks around 1.5 and 3°.

S2.   FEM simulations

Finite element method (FEM) simulations were performed in order to assess if the dielectric spacer layers affect the electrical characterization. The concern is that the MgO and $MgFe_2O_4$layers could reduce the amount of charge carriers penetrating to the lower layers, thus limiting electrical mea-
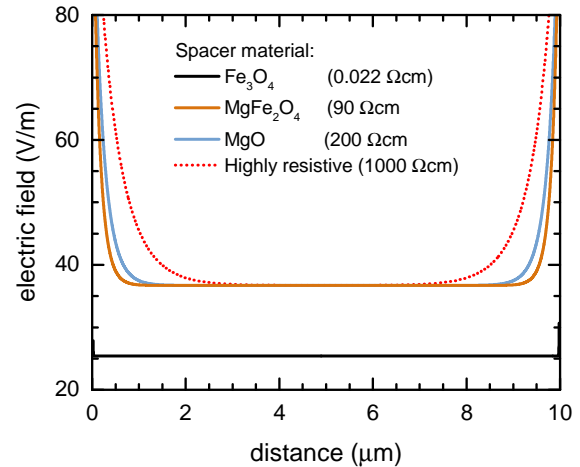

Supplementary Figure S1. The magnitude of electric field along the top surface of the substrate. The electric field at the substrate surface and hence the lower side of the bottom most layer saturates 1 μm away from the contact. As contacts are spaced 2 mm apart in real samples a potential effect of injecting carriers only in the top most layer on sheet resistance measurements can therefore be neglected.

surements to the first layer. The system can be modelled simply in two dimensions, treating the direction along the gold contacts as infinite. A 30 μm wide section of 30 nm thick substrate with layers of 3-2-3-2-3 nm was simulated. The 3 nm layers were given a resistivity of 0.022 Ω cm, the substrate was given a resistivity of 200 Ω cm and a number of resistivities were checked for the buffer layer (0.022, 90, 200 and 1000 Ω cm). An input boundary current was injected at the top surface on one end of the sample and allowed to leave through the top surface at the other end.

In these simulations, even with a resistivity of 1 kΩcm, the current was evenly distributed throughout the 3 nm layers in the centre of the substrate. In order to see what distance it took for the current to become fully distributed one can look at the electric field along the surface. If the electric field is constant along the top surface then so is the current and it must be distributed evenly throughout the layers. This can be seen in figure S1, where we can see that in all cases the current has become equally distributed after 3 μm. Given that we wouldn't expect a resistivity greater 1 kΩcm and the distances from the outer injection contacts to the voltage contacts on the substrates was on the order of mm, penetration of charge carriers should not affect the measurements.

S3.   Additional resistance data

Our sample geometry allows for the measurements of the electrical properties of the ultrathin films and multilayers. In Fig. S2 we show the resistance vs. temperature data for all
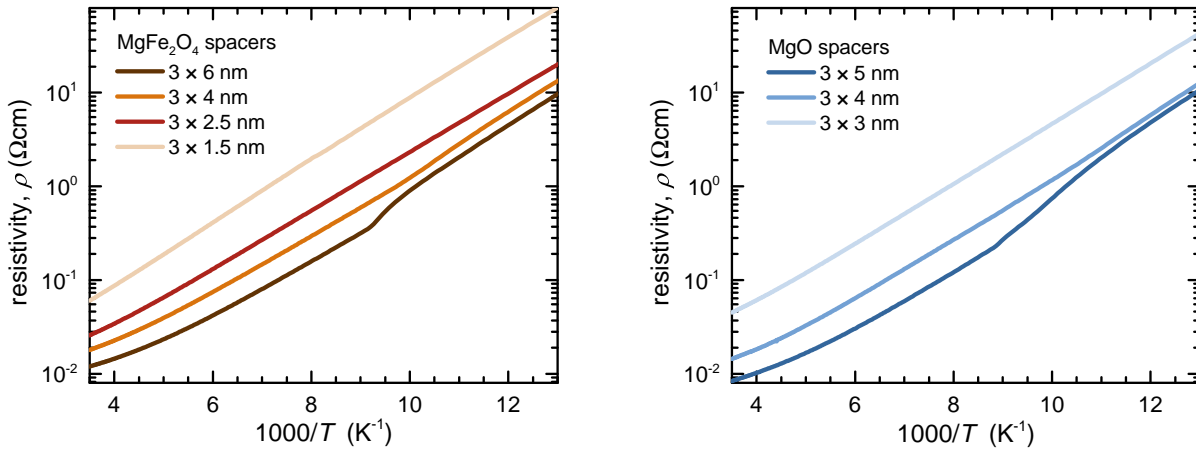
Supplementary Figure S2. Resistance vs. Temperature measurements. On the left is the sample set with $MgFe_2O_4$ spacer layers, on the right those with MgO.

samples where magnetisation measurements where available.

In contrast to the MR, magnetisation and Raman data, the small deviations in the resistivity between the sets with MgO and $MgFe_2O_4$ spacers can not be directly assigned to possible differences in the structure of the thin films grown with different spacer material. The errors of the thickness determination and slight variations in growth rate between different runs, the small deviations in the resistivity between the sets with MgO and $MgFe_2O_4$ spacer could solely be responsible for the observed differences.

S4. Deconvolution of substrate and thin film Raman data

For samples grown on MgO substrates the measured Raman spectra can be directly used for data analysis and Raman peak fitting. For samples grown on $SrTiO_3$ substrates the strong Raman modes of the substrate make analysis much more difficult. The Fe_3O_4 A_{1g} mode is coinciding with broad peaks originating from the $SrTiO_3$. In order to extract the weak Fe_3O_4 signal from the background the following strategy has been employed. Figure S3 illustrates this for one sample.

1. The plain substrate has been measured for each sample on a small area not covered by the thin film. This ensured that any potential differences in the substrate Raman spectra due to the annealing procedures is not wrongly interpreted as a thin film signal.

2. The area with the Fe_3O_4 film was measured using the same integration time.

3. The signal in the area between 200-600 cm^{-1} was integrated and the thin film measurement was normalised to have the same area count as the substrate. This was required to account for drifts in laser power and more importantly microscope focus during the long integration measurements (typically 20 min). The area was chosen to exclude the low frequency range as it potentially could be affected by differences in sample roughness (elastically scattered laser light), as well as the area of the main Fe_3O_4 peak itself.

4. The difference between the area normalised thin film and substrate measurements reveals the Raman modes

of the thin film. The latter was then analysed in the same way as the raw measurements for films on MgO.
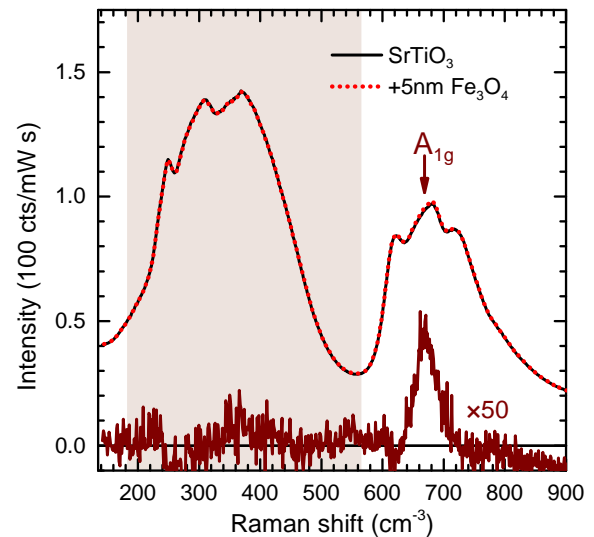
Supplementary Figure S3. Data processing to extract the weak Fe_3O_4 Raman signal for samples grown on $SrTiO_3$: Raw measurements of areas with and without the thin film were area normalised in the marked range. The difference between the measurements is the Fe_3O_4 signal.

Supplementary Table S1. List of the sample set, their nominal superlattice structure, the individual layer thickness as determined by fits to X-ray reflection measurements, and the measured Verwey transition for each layer. For the thinnest single layers (marked *) $d_{Fe_3O_4}$ was estimated using the average difference between nominal and measured thickness, as they were to thin for XRR analysis. The transition temperature T_v was defined as the point of maximum slope change of the $\ln(\rho)$ vs. Temperature curve (maximum in the 2nd derivative).

Sample ID	Geometry (nominal)	$d_{Fe_3O_4}$ (from XRR)	d_{spacer} (from XRR)	T_v
	Multilayers with **MgO** spacers			
K15-A	$\left[Fe_3O_{4(\mathbf{6\,nm})}/MgO_{(2\,nm)}\right]_3$	6.3 nm	1.9 nm	110±3 K
K4-A	$\left[Fe_3O_{4(\mathbf{5\,nm})}/MgO_{(2\,nm)}\right]_3$	5.0 nm	1.7 nm	112±3 K
K3-A	$\left[Fe_3O_{4(\mathbf{4\,nm})}/MgO_{(2\,nm)}\right]_3$	3.6 nm	1.8 nm	95±3 K
K2-A	$\left[Fe_3O_{4(\mathbf{3\,nm})}/MgO_{(2\,nm)}\right]_3$	2.5 nm	1.6 nm	-
K5-A	$\left[Fe_3O_{4(\mathbf{1.5\,nm})}/MgO_{(2\,nm)}\right]_3$	1.2 nm	1.7 nm	-
	Multilayers with **MgFe$_2$O$_4$** spacers			
I6-A	$\left[Fe_3O_{4(\mathbf{6\,nm})}/MgFe_2O_{4(1.5\,nm)}\right]_3$	5.9 nm	1.4 nm	108.5±1 K
I3-A	$\left[Fe_3O_{4(\mathbf{4\,nm})}/MgFe_2O_{4(1.5\,nm)}\right]_3$	4.2 nm	1.4 nm	107±4 K
I2-A	$\left[Fe_3O_{4(\mathbf{2.5\,nm})}/MgFe_2O_{4(1.5\,nm)}\right]_3$	2.5 nm	1.5 nm	-
I4-A	$\left[Fe_3O_{4(\mathbf{1.5\,nm})}/MgFe_2O_{4(1.5\,nm)}\right]_3$	1.4 nm	1.3 nm	-
	Single layer, Fe$_3$O$_4$ thin films			
K15-B	$Fe_3O_{4(\mathbf{18\,nm})}$	19.6 nm	-	113±1 K
I6-B	$Fe_3O_{4(\mathbf{18\,nm})}$	17.6 nm	-	113±1 K
K4-B	$Fe_3O_{4(\mathbf{15\,nm})}$	15.5 nm	-	113±1 K
K3-B	$Fe_3O_{4(\mathbf{12\,nm})}$	11.8 nm	-	112±1 K
I3-B	$Fe_3O_{4(\mathbf{12\,nm})}$	12.2 nm	-	112±2 K
K2-B	$Fe_3O_{4(\mathbf{9\,nm})}$	8.3 nm	-	108±2 K
I2-B	$Fe_3O_{4(\mathbf{7.5\,nm})}$	7.5 nm	-	110±2 K
K5-B	$Fe_3O_{4(\mathbf{4.5\,nm})}$	3.7 nm	-	-
I4-B	$Fe_3O_{4(\mathbf{4\,nm})}$	4.0 nm	-	-
I5-A	$Fe_3O_{4(\mathbf{2.5\,nm})}$	*2.4 nm	-	-
I5-B	$Fe_3O_{4(\mathbf{1.5\,nm})}$	*1.4 nm	-	-
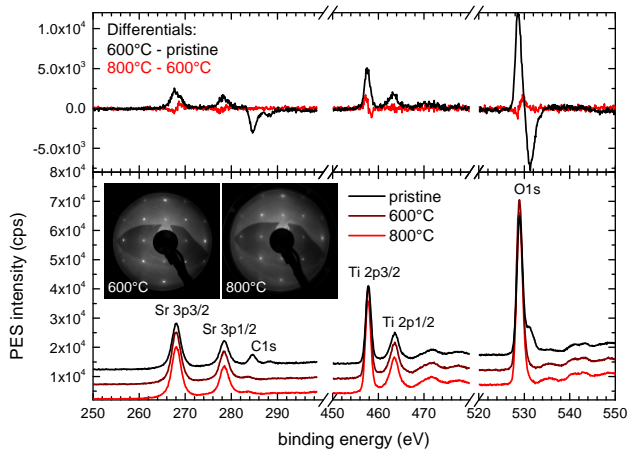
Supplementary Figure S4. *in-situ* Characterisation of the STO substrate: XPS spectra of the pristine, 600°C and 800°C annealed STO(100) substrates. The main changes during vacuum annealing occur already at 600°C removing any residual carbon and hydroxide contamination. Further annealing at 800°C did not lead to significant changes of the surface stoichiometry or long range surface order as the XPS spectra do not change and the surface remains 1×1 reconstructed. The measurements have been performed in an Omicron MultiProbeXP using a monochromised Al Kα source.
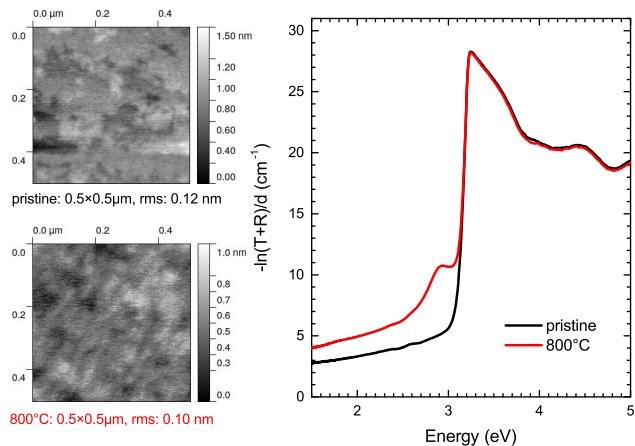
Supplementary Figure S5. *ex-situ* Characterisation of the STO substrate: AFM micrographs of the pristine and 800°C annealed reveal no changes in the overall rms roughness of the substrates. The optical absorption as determined from transmission (T) and reflectance measurements (R) illustrate the increased absorption below the STO band gap once oxygen vacancies are present. Optical measurements have been performed on single sided polished STO in a PerkinElmer 650S spectrophotometer, equipped with an integrating sphere, AFM measurements where performed in tapping mode using an ND-MDT Solver Pro AFM.

S5. STO surface characterisation

We attribute the altered magnetic moment of an ultrathin Fe_3O_4 film on STO substrates annealed at 600°C and 800°C to the increased density of oxygen vacancies in the substrate causing a reduction of the thin Fe_3O_4. In doing so, we have to exclude the possibility that the morphology of the surface is significantly altered in the annealing process. Vacuum annealing of the STO(001) surface has been extensively studied previously. In this work we follow the process of 30 min vacuum annealing steps as thoroughly investigated by Dagdeviren *et al.*.[1] Under these conditions no changes in the step density of the STO(001) surface was observed, while the increased density of oxygen vacancies lead to a change in surface reconstructions. In contrast to this work we did not perform extensive ex-situ cleaning steps involving either oxygen annealing and/or acid treatment required to achieve large, regular terraces. Hence our surfaces will show higher step densities and no defined long range order, leading to defined LEED patterns. Hence we observe only a 1×1 LEED pattern for both the 600°C and 800°C sample, with no changes in the rms roughness measured *ex-situ* before and after vacuum annealing. The main effect of the vacuum anneal is the removal of residual surface carbon and surface hydroxide. As confirmed by XPS, this process is complete at 600°C and no significant difference in the surface stoichiometry is seen in XPS measurements (see Fig. S4). The only significant difference found in the sample annealed at the higher temperature of 800°C is a discoloration of the bulk of the substrate as seen in additional absorption structures below the band gap (see Fig. S5) as expected for oxygen vacancies.[2] Our supplementary measurements confirm that the only significant change between vacuum annealing at 600°C and 800°C is the formation of bulk oxygen vacancies, consistent with previous investigations.[3] The annealing steps performed here are not severe enough to introduce morphology and stoichiometry changes, e.g. surface phase segregation as seen in other reports.[4] This is substantiated by our XPS measurements, where no significant changes in the Ti/Sr ratio was found.

[1] O. E. Dagdeviren, G. H. Simon, K. Zou, F. J. Walker, C. Ahn, E. I. Altman, and U. D. Schwarz, Phys. Rev. B **93**, 195303 (2016).

[2] C. Mitra, C. Lin, J. Robertson, and A. A. Demkov, Phys. Rev. B **86**, 155105 (2012).

[3] D. Schwarz and H. Anderson, J. Electrochem. Soc. **122**, 707 (1975).

[4] K. Szot and W. Speier, Phys. Rev. B **60**, 5909 (1999).